The Astrophysical Journal, 839:53 (10pp), 2017 April 10 https://doi.org/10.3847/1538-4357/aa6974

A Numerical Study of Forbush Decreases with a 3D Cosmic-Ray Modulation Model Based on an SDE Approach

Xi Luo[1,2], Marius S. Potgieter[2], Ming Zhang[3], and Xueshang Feng [1]
[1] SIGMA Weather Group, State Key Laboratory of Space Weather, National Space Science Center, Chinese Academy of Sciences, Beijing 100190, China
[2] Centre for Space Research, North-West University, Potchefstroom 2520, South Africa
[3] Department of Physics and Space Sciences, Florida Institute of Technology, 150 West University Boulevard, Melbourne, FL 32901, USA
Received 2017 January 3; revised 2017 March 23; accepted 2017 March 24; published 2017 April 13

Abstract

Based on the reduced diffusion mechanism for producing Forbush decreases (Fds) in the heliosphere, we constructed a three-dimensional (3D) diffusion barrier, and by incorporating it into a stochastic differential equation (SDE) based time-dependent, cosmic-ray transport model, a 3D numerical model for simulating Fds is built and applied to a period of relatively quiet solar activity. This SDE model generally corroborates previous Fd simulations concerning the effects of the solar magnetic polarity, the tilt angle of the heliospheric current sheet (HCS), and cosmic-ray particle energy. Because the modulation processes in this 3D model are multi-directional, the barrier's geometrical features affect the intensity profiles of Fds differently. We find that both the latitudinal and longitudinal extent of the barrier have relatively fewer effects on these profiles than its radial extent and the level of decreased diffusion inside the disturbance. We find, with the 3D approach, that the HCS rotational motion causes the relative location from the observation point to the HCS to vary, so that a periodic pattern appears in the cosmic-ray intensity at the observing location. Correspondingly, the magnitude and recovery time of an Fd change, and the recovering intensity profile contains oscillation as well. Investigating the Fd magnitude variation with heliocentric radial distance, we find that the magnitude decreases overall and, additionally, that the Fd magnitude exhibits an oscillating pattern as the radial distance increases, which coincides well with the wavy profile of the HCS under quiet solar modulation conditions.

Key words: cosmic rays – Sun: activity – Sun: heliosphere

1. Introduction

Using ionization chambers, Forbush (1937) found that the cosmic-ray intensity at the Earth decreased during a magnetic storm and the decrease lasted for several days. After that, the term Forbush decrease (Fd) has been used to represent most short-term transients in cosmic-ray intensity in the heliosphere (see e.g., Cane 2000). In this paper, we focus on the classical Fd, which has a sharp decrease in intensity, typically within a day, followed by a gradual recovery to previous intensity levels over several days.

The basic mechanism for causing Fds has been studied using various observations over many years (Simpson 1954; Morrison 1956; Barouch & Burlaga 1975; Zhang & Burlaga 1988; Sarris et al. 1989; Cheng et al. 1990; Lockwood et al. 1991; Yu et al. 2010). For example, Simpson (1954) showed that Fd-type intensity variations observed at the Earth were not produced by geomagnetic field disturbance and Morrison (1956) proposed that they were caused by turbulent magnetic plasma emitted from the Sun. Barouch & Burlaga (1975) found that most Fd were associated with interplanetary magnetic field (IMF) enhancements. Zhang & Burlaga (1988) did a statistical study of the relationship between magnetic clouds and Fd. They found that the clouds, associated with strong Fd events, were preceded by interplanetary shocks. It was inferred that the turbulent sheath region behind the preceding shock caused the Fd. Lockwood et al. (1991) performed an elaborate investigation of Fd and restated that the main phase of an Fd happened when the turbulent sheath region passed the Earth. Their observational analysis strongly suggests that the Fd was mainly produced by reduced particle diffusion in the turbulent region behind the shock. Recent studies by Yu et al. (2010) and Arunbabu et al. (2015) also support this scenario. Although particle drift near a shock may play a role in forming Fd (Sarris et al. 1989; Cheng et al. 1990), we assume that the basic mechanism for Fd is the reduced diffusion inside the associated turbulent region, acting as a propagating cosmic-ray barrier. This assumption constitutes the basis for our numerical modeling.

Numerical simulations, which focused on the physical causes and basic features of Fds and were done with increasing complexity, have also been reported over the years (Nishida 1982; Thomas & Gall 1984; Kadokura & Nishida 1986; le Roux & Potgieter 1989, 1991; Wawrzynczak & Alania 2010). For example, Nishida (1982) solved a 1D diffusion–convection transport equation and studied the precursory increase during an Fd event. Following their previous work, Kadokura & Nishida (1986) built a 2D cosmic-ray transport model for studying Fd by using a diffusion barrier with the full latitude extent. Because particle drift was included in their model, they found that the effect of the solar magnetic polarity was more pronounced in the polar regions of the heliosphere and that the magnitude of an Fd was larger during the positive polarity epoch. Concurrently, using a perturbation approach to determine the time variation of the diffusion coefficient, Chih & Lee (1986) performed an insightful analytical investigation, obviously restricted to 1D, that we shall discuss again below.

Using a Monte-Carlo simulation, Thomas & Gall (1984) argued that the prolonged containment of cosmic rays inside the turbulent sheath region could cause additional adiabatic cooling, such as the principal mechanism for causing Fd. They showed that an eastward directed shock produces large Fd and that larger diffusion coefficients caused the Fd magnitude to decrease. In addition, they reported that the Fd profile would change if the propagating shock had a full spherical extent.

Adapting the scenario that an Fd is caused by a propagating diffusion barrier, le Roux & Potgieter (1991) solved the 2D transport equation, including adiabatic cooling and particle drift. Their model predicts that the recovery time is longer when the polarity of the solar magnetic field is negative, comparing with the recovery time during the positive epoch. In addition, they showed that the polarity-reversal effect gets reduced as the tilt angle of the heliospheric current sheet (HCS) increases. More recently, Wawrzynczak & Alania (2010) studied the features of Fds using observational data in comparison with their numerical model, focussing on the time-dependent changes of the rigidity spectrum exponent for Fds at rigidities of 10 GV.

Although the "reduced diffusion" mechanism for Fds is widely accepted, the concept has not been applied in a full 3D, time-dependent, numerical model to simulate it. This is probably because of the difficulty of solving the time-dependent, cosmic-ray transport equation using standard finite-difference numerical methods, particularly one that includes all major modulation mechanisms, together with the complexity of a propagating diffusion barrier as well as a rotating wavy HCS. Codes for solving partial differential equations with five numerical dimensions (3D space, energy, and time) are not unconditionally stable. However, with the development of the Markov Stochastic Method, as discussed below, we now report and utilize here a full 3D, time-dependent, Stochastic Differential Equation (SDE) model for studying Fds. New features, revealed by this 3D approach are illustrated and discussed.

We first describe the SDE model, specifically giving details of how the time-dependent aspects are handled and how the 3D propagating diffusion barrier is constructed. We then compare our 3D simulations with previous results as a validation of our SDE approach. Some interesting new aspects of Fd features are also illustrated. In the final section, we summarize and make conclusions.

2. Numerical Method

2.1. Time-dependent 3D Numerical Cosmic-ray Transport Model

In this section, we describe the cosmic-ray transport equation and briefly discuss how it is solved numerically using the SDE approach. This is followed by an explanation of how the propagating diffusion barrier is defined in 3D and how it is constructed.

2.1.1. The Cosmic-ray Transport Equation and the Stochastic Method

Parker (1965) derived the following equation for cosmic-ray propagation in the heliosphere based on the Fokker–Plank equation,

$$\frac{\partial f}{\partial t} = -(\boldsymbol{V}_{\rm sw} + \langle \boldsymbol{v}_{\rm d}\rangle)\cdot\nabla f + \nabla\cdot(K^{(s)}\cdot\nabla f) + \frac{1}{3}(\nabla\cdot\boldsymbol{V}_{\rm sw})\frac{\partial f}{\partial \ln p}. \quad (1)$$

Here, $f(\boldsymbol{r}, p, t)$ is the isotropic distribution function or phase-space density as a function of spatial position $\boldsymbol{r}$, momentum p, and time t. The cosmic-ray intensity $j_T \propto p^2 f$. $\boldsymbol{V}_{\rm sw}$ is the solar wind velocity, and $\langle \boldsymbol{v}_{\rm d}\rangle$ is the pitch-angle averaged drift velocity (e.g., Jokipii et al. 1977; Burger & Potgieter 1989) over the near-isotropic particle distribution, which can be written as

$$\langle \boldsymbol{v}_{\rm d}\rangle = \nabla\times\kappa_T\hat{e}_B. \quad (2)$$

which reduces to $\kappa_T = pv/3qB$ if weak scattering is assumed (e.g., Forman et al. 1974; Engelbrecht & Burger 2015; Ngobeni & Potgieter 2015), with q and v the cosmic-ray particle's charge and speed. Here, $K^{(s)}$ is the diffusion tensor, and it can be expressed as

$$K^{(s)} = \begin{pmatrix} \kappa_{\parallel} & 0 & 0 \\ 0 & \kappa_{\perp\theta} & 0 \\ 0 & 0 & \kappa_{\perp r} \end{pmatrix}, \quad (3)$$

in the local interplanetary (or heliospheric) magnetic field coordinate system. Our study focuses on galactic protons with kinetic energy $E \leqq 1$ GeV.

For simplicity, we choose the following forms for the parallel $\kappa_{\parallel}$ and two perpendicular diffusion coefficients $\kappa_{\perp\theta}$ and $\kappa_{\perp r}$:

$$\kappa_{\parallel} = \kappa_{\parallel 0}\beta\left(\frac{p}{p_o}\right)^{0.5}\frac{B_{\rm eq}}{B}, \quad (4)$$

$$\kappa_{\perp\theta} = \kappa_{\perp r} = \kappa_{\perp 0}\beta\left(\frac{p}{p_o}\right)^{0.5}\frac{B_{\rm eq}}{B}, \quad (5)$$

where β is the ratio of the particle's speed to the speed of light and p is particle momentum in the unit of GeV/c with $p_o = 1$ GeV/c. The IMF magnitude B is in units of nT, and $B_{\rm eq}$ is the value at the Earth. In our simulation, $\kappa_{\parallel 0} = 50\times 10^{20}$ cm^2 s^{-1} and $\kappa_{\perp 0} = 2\times 10^{20}$ cm^2 s^{-1}, unless otherwise stated.

Based on the Ito formula, Equation (1) can be arranged to the following set of stochastic differential equations (Zhang 1999; Kopp et al. 2012):

$$d\boldsymbol{X} = (\nabla\cdot K^{(s)} - \boldsymbol{V}_{\rm sw} - \langle \boldsymbol{v}_D\rangle)ds + \sum_{\sigma=1}^{3}\boldsymbol{\alpha}_\sigma dW_\sigma(s),$$
$$dP = \frac{1}{3}P(\nabla\cdot\boldsymbol{V}_{\rm sw})ds. \quad (6)$$

Here, $\sum_\sigma \alpha_\sigma^\mu\alpha_\sigma^\nu = 2\kappa^{\mu\nu}$, and $dW_\sigma(s)$ is the Wiener process. Equation (6) describes the random trajectory for the stochastic variable $\boldsymbol{Q} = (\boldsymbol{X}, P)$. With the help of the Ito formula, Zhang (1999) showed that the solution to the cosmic-ray transport Equation (1) can be written as

$$f(t, \boldsymbol{Q}) = \langle f_b(t-\chi, \boldsymbol{Q}_\chi)\rangle, \quad (7)$$

where χ is the first exit time for the stochastic process to get to the outer boundary, with the boundary value of $f_b(t-\chi, \boldsymbol{Q}_\chi)$. It should be noted that the time t is already an intrinsic variable in the stochastic process for $\boldsymbol{Q}$. Thus, Equations (6) and (7) automatically lead to a time-dependent cosmic-ray transport model. See also Luo et al. (2011, 2013) for detailed information and references.

In order to obtain the value of the distribution function at $(t, \boldsymbol{X}, p)$, a large number of (N) stochastic processes, all starting from this point defined by Equation (6), are generated. For each of them, the first exit value $(\boldsymbol{X}_i, p_i)$ is recorded, with the corresponding boundary value of $f_b^i(t-\chi_i, \boldsymbol{X}_i, p_i)$, and then

follows $f(t, \boldsymbol{X}, p) = \sum_i f_b^i(t - \chi_i, \boldsymbol{X}_i, p_i)/N$. The solution to the cosmic-ray transport equation is just the expectation value of all boundary values when stochastic processes exit.

For studying Fds, we are concerned with the relative cosmic-ray intensity, which is not affected by the exact form of the local interstellar spectrum (Luo et al. 2013), specified at the the outer boundary. Thus, we still adopt the previously used form for this study (Zhang 1999):

$$f_{\rm ism}(p) \propto (m_0^2 c^2 + p^2)^{-1.8}/p, \tag{8}$$

where m_0 is the rest mass of a proton. As for the inner boundary, an absorbing boundary condition is used where pseudo-particles, when reaching the solar surface, exit the simulation domain.

2.1.2. Model for IMF and Current Sheet Drift

In our numerical simulation, the Parker's IMF model with sector structure is utilized:

$$\boldsymbol{B}(r, \theta) = \frac{A}{r^2}\left(\hat{e_r} - \frac{r\Omega \sin\theta}{V_{\rm sw}}\hat{e_\phi}\right)[1 - 2H(\theta - \theta_{\rm cs})], \tag{9}$$

where r is the radial distance to the Sun, Ω is the solar rotation angular speed, and $V_{\rm sw}$ is the solar wind speed. In the simulation, the solar wind is set to be a radially outward stream, i.e., $\boldsymbol{V}_{\rm sw} = V_{\rm sw}\hat{e_r}$. An ideal termination shock is placed at 92 au. Inside the termination shock ($r < 92$ au), $V_{\rm sw} = 400$ km s^{-1}. Outside the termination shock ($r > 92$ au), it decreases according to $V_{\rm sw} = 120 \times (92/r)^2$ km s^{-1}. $H(\theta - \theta_{\rm cs})$ is the Heaviside function and $\theta_{\rm cs}$ determines the polar extent of the HCS. Following Kóta & Jokipii (1983), the wavy HCS is modeled according to the analytical form

$$\cot(\theta_{\rm cs}) = -\tan(\alpha)\sin(\phi^*), \tag{10}$$

where α is the tilt angle of the HCS, $\phi^* = \phi + \frac{r\Omega}{V_{\rm sw}}$. An additional term $-\Omega t$, which is the phase of the co-rotating HCS, may also be added to rotate the HCS. The effect of this term will be studied in the following sections. Here, (r, $\theta_{\rm cs}$, ϕ) define the shape of the HCS's wavy surface.

In Equation (9), A is a constant that indicates the strength and polarity of the IMF model. It is set to $B = 5$ nT at the Earth's orbit ($r = 1$ au, $\theta = 90°$, $\phi = 0°$), so that the $A = \pm 5\Big/\sqrt{\left(1 + \frac{\Omega^2}{V_{\rm sw}^2}\right)}$. The sign of A is determined by the polarity of the solar magnetic field. For an elaborate discussion of alternative approaches to the IMF model, see Raath et al. (2016).

Following Burger & Potgieter (1989), the magnitude of the particle drift velocity in the HCS is specified as

$$v_{\rm ns} = \frac{v}{6} \times \frac{4R_{\rm g}}{r}\delta(\theta - \theta_{\rm cs}), \tag{11}$$

where $R_{\rm g}$ is the gyroradius of the cosmic-ray particle, r is again the radial distance, and v is particle speed; see also Jokipii et al. (1977), Kóta & Jokipii (1983), Potgieter & Moraal (1985), Strauss et al. (2012). Assuming cosmic-ray particles experience this singular drift within a distance $xR_{\rm g}$ (usually $x = 2$) from the HCS, and $xR_{\rm g} = r\epsilon$, the following relationship is obtained:

$$\int_{\theta-\epsilon}^{\theta+\epsilon} \delta(\theta - \theta_{\rm cs})d\theta = 1 = \int_{\theta-\epsilon}^{\theta+\epsilon} \frac{r}{2xR_{\rm g}}d\theta. \tag{12}$$

The function $\delta(\theta - \theta_{\rm cs})$ is approximated by $r/(2xR_{\rm g})$ within the distance of $(-xR_{\rm g}, xR_{\rm g})$ to the HCS. By defining ζ as the angle between the local current sheet normal direction $\hat{n}$ and the $-\hat{e}_\theta$ direction, the current sheet drift vector can be written as

$$\boldsymbol{V}_{\rm cs} = \frac{v}{3x}(\sin\Phi\cos\zeta\hat{e}_r + \sin\zeta\hat{e}_\theta + \cos\Phi\cos\zeta\hat{e}_\phi), \tag{13}$$

with Φ the IMF winding (spiral) angle. If a locally flat HCS is assumed, the distance d to the HCS can also be approximated as

$$d = |r(\theta - \theta_{\rm cs})\cos\zeta|. \tag{14}$$

See also the description by Strauss et al. (2012).

2.2. The Diffusion Barrier Model

A propagating diffusion barrier is described by the following function, which defines its 3D geometrical profile:

$$\kappa'_{\parallel,\perp,T} = \frac{\kappa_{\parallel,\perp,T}}{[1 + \rho h(\theta)f(r)g(\phi)]}. \tag{15}$$

Here, $\kappa'_{\parallel,\perp,T}$ represents the diffusion and drift coefficients inside the diffusion barrier, ρ is a constant determining the reduction level of the diffusion coefficient magnitude inside the barrier and $h(\theta)$ and $g(\phi)$ determine the geometry of the diffusion barrier. In terms of the polar angle θ and azimuthal angle ϕ, they are prescribed as

$$h(\theta) = e^{-\left(\frac{\theta-\pi/2}{\theta_{\rm br}}\right)^{10}}, \tag{16}$$

$$g(\phi) = e^{-\left(\frac{\phi}{\phi_{\rm br}}\right)^{10}}. \tag{17}$$

The values of $\theta_{\rm br}$ and $\phi_{\rm br}$ specify the maximum extent of this diffusion barrier along the $\hat{e_\theta}$ (polar) and $\hat{e_\phi}$ (azimuthal) directions.

The radial profile of this diffusion barrier is given by

$$f(r) = \begin{cases} 1 - \frac{r - r_{\rm cen}}{r_a} & \text{if } r_{\rm cen} < r < r_{\rm sh} \\ \frac{r - r_{\rm end}}{r_b} & \text{if } r_{\rm end} < r \leqslant r_{\rm cen}, \end{cases} \tag{18}$$

where $r_{\rm sh}$ ($r_{\rm end}$) is the radial distance for the barrier's front (end) location, and $r_a = r_{\rm sh} - r_{\rm cen}$, $r_b = r_{\rm cen} - r_{\rm end}$ are widths of leading and trailing paths of the barrier respectively. The total width (radial extent) of the barrier is $L = r_a + r_b = r_{\rm sh} - r_{\rm end}$. According to Equation (15), both diffusion and particle drift are reduced inside this barrier. As for the propagation profile, we assume the barrier moves with a constant speed $V_{\rm br}$ ($V_{\rm br} > V_{\rm sw}$) radially outward. Based on an estimation for the associated shock speed of a global merged interaction region (Luo et al. 2011), and the statistical analysis for the speeds of coronal mass ejections (Yurchyshyn et al. 2005), $V_{\rm br}$ is set to be 508 km s^{-1}. The plasma speed inside the barrier is changed according to $V_{\rm p} = V_{\rm br} - V_{\rm sw}/(1 + \rho h(\theta)f(r)g(\phi))$.

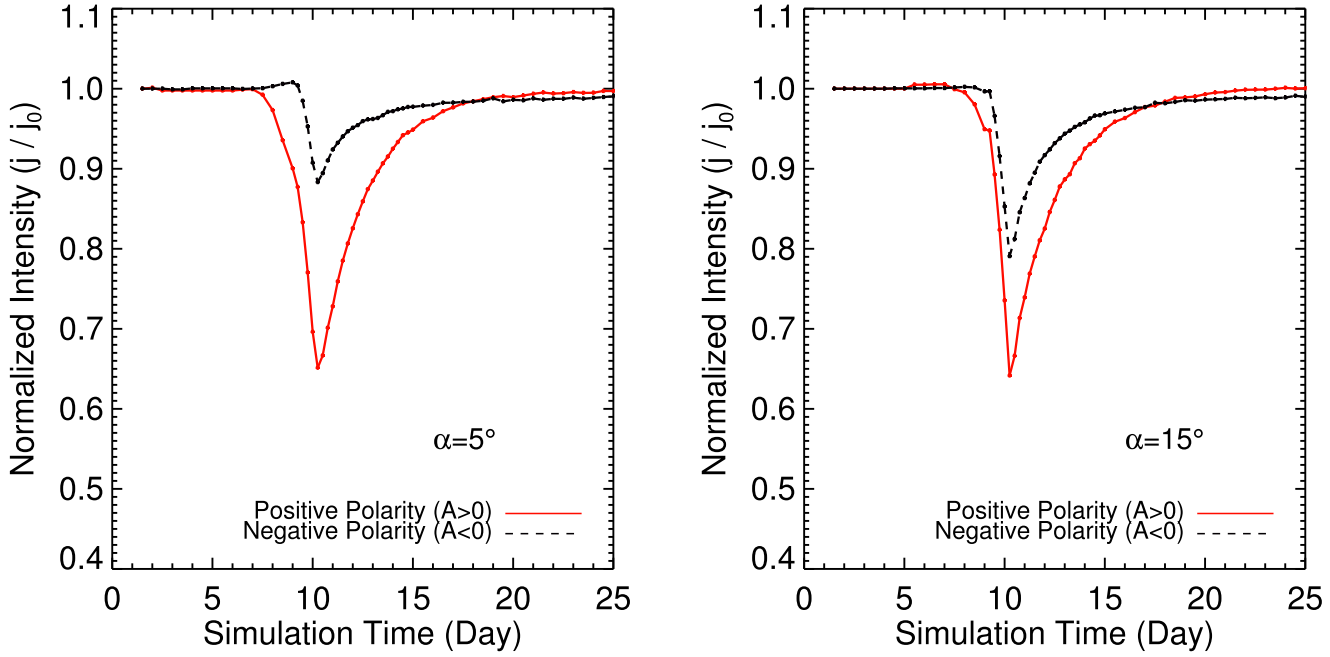

Figure 1. Simulated Fd profile for 1.0 GeV protons for the two polarity epochs of the solar magnetic field. The intensity is normalized to the undisturbed value before the passage of the Fd. In the left panel, the tilt angle is set to $\alpha = 5°$ and in the right panel to $\alpha = 15°$.

3. Results and Discussion

3.1. Comparison with 2D Fd Models

Our 3D SDE model has been tested and validated by a comparison of results to previous simulations obtained with 2D models (Thomas & Gall 1984; Kadokura & Nishida 1986; le Roux & Potgieter 1989, 1991).

3.1.1. Effect of the Sun's Magnetic Field Polarity

Simulating the time varying intensity near the Earth (1 au, $\theta = 90°$, $\phi = 0°$), we obtain an Fd profile as shown in Figure 1. For this profile, the full parameter set as described above is $\rho = 3.0$, $L = 0.5$ au, $\theta_{\rm br} = 45°$, $\phi_{\rm br} = 150°$, $\kappa_\perp/\kappa_\parallel = 0.04$, and $\kappa_{\parallel 0} = 50 \times 10^{20}$ cm^2 s^{-1}. Since our study is mainly illustrative, the cosmic-ray intensity is normalized to the undisturbed value j_0 before the passage of the diffusion barrier. In the left panel of Figure 1, we set $\alpha = 5°$. The solid red curve is the simulation with the solar magnetic field pointing outward in the northern hemisphere, the so-called $A > 0$ polarity epochs, and the dashed brown curve when $A < 0$. For the right panel $\alpha = 15°$ to illustrate how the magnitude of the Fd responds to an increase in tilt angle.

Following Lockwood & Webber (1986) and le Roux & Potgieter (1991), we define the magnitude of the Fd as $(j_0 - j_{\rm m})/j_0$, where $j_{\rm m}$ is the minimum cosmic-ray intensity during the Fd event. The recovery phase of the Fd can be fitted by the following function.

$$j(t) = j_0 - (j_0 - j_{\rm m})e^{-(t-t_{\rm m})/\tau}, \quad (19)$$

where $t_{\rm m}$ is the time when the cosmic-ray intensity reaches a minimum value $j_{\rm m}$; the constant τ is defined as the recovery time, when the intensity decrease level $j_0 - j(\tau)$ returns to e^{-1} of the its maximum decreased level $j_0 - j_{\rm m}$.

In Table 1, the computed magnitude and recovery time for these Fd profiles according to Figure 1 are shown. Based on these results, several points are emphasized. (1) The magnitude of the Fd is larger during the $A > 0$ epoch than during $A < 0$, for both $\alpha = 5°$ and $\alpha = 15°$. In addition, the difference in the Fd magnitude for the two epochs decreases as the tilt angle increases. During the $A < 0$ cycle, positively charged cosmic-ray particles enter the inner heliosphere through the equatorial plane. Because current sheet drift provides easy access to the inner heliosphere, the effect of the diffusion barrier is weakened. Previous simulations also revealed a larger Fd magnitude in the $A > 0$ cycle (Kadokura & Nishida 1986) and a smaller Fd magnitude for larger tilt angles during the $A < 0$ cycle (le Roux & Potgieter 1989). (2) For both $\alpha = 5°$ and $\alpha = 15°$, the recovery time is about the same during different polarity epochs, though for the larger tilt angle the difference becomes somewhat larger. The relatively small differences are in contrast to the 2D simulations of le Roux & Potgieter (1989, 1991) who predicted that the recovery time of an Fd should always be significantly longer when $A < 0$. In this context, it is reasonable to argue that since all mechanisms in the azimuthal plane are neglected by assumption in the 2D approach, the effects on the Fd profile is exaggerated in 2D. In fact, the observed polarity effect on the recovery time of Fds was found to be quite small, barely statistically significant (Mulder & Moraal 1986), in contrast to the simulations of le Roux & Potgieter (1991) but apparently in accordance to what our 3D approach predicts.

Table 1
The Magnitude and Recovery Times for Fd Profiles Shown in Figure 1

	Magnitude	Recovery Time (in days)
$A > 0$ $\alpha = 5°$	0.35	2.51
$A < 0$ $\alpha = 5°$	0.12	2.52
$A > 0$ $\alpha = 15°$	0.36	2.40
$A < 0$ $\alpha = 15°$	0.21	2.15

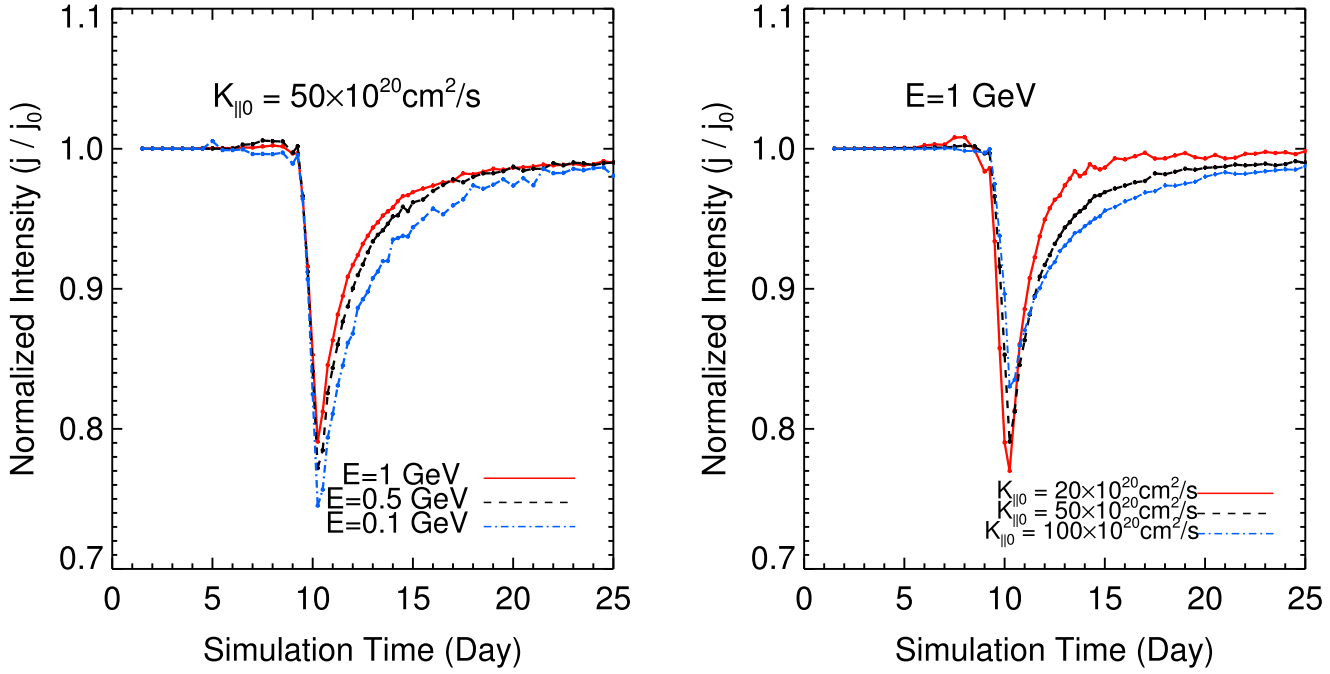

Figure 2. Left panel shows the simulated Fd profile for 1, 0.5, and 0.1 GeV protons, when $\kappa_{\parallel 0} = 50 \times 10^{20}$ cm^2 s^{-1}. The right panel shows the results for 1.0 GeV protons when $\kappa_{\parallel 0} = 20 \times 10^{20}$ cm^2 s^{-1}, $\kappa_{\parallel 0} = 50 \times 10^{20}$ cm^2 s^{-1}, and $\kappa_{\parallel 0} = 100 \times 10^{20}$ cm^2 s^{-1}.

3.1.2. Effect of Changed Diffusion Coefficients and Cosmic-Ray Energy

In Figure 2, two different Fd profiles are simulated by changing the cosmic particle's kinetic energy (E, left panel) and the value of $\kappa_{\parallel 0}$ (right panel). The parameter set is $\rho = 3.0$, $L = 0.5$, $\theta_{\rm br} = 45°$, $\phi_{\rm br} = 150°$, and $\kappa_\perp/\kappa_\parallel = 0.04$, with $A < 0$ and $\alpha = 15°$. The computed magnitude and recovery time according to the Fd profiles in Figure 2 are listed in Table 2. Both Fd magnitude and recovery time decrease when E is increased from 0.1 to 1.0 GeV (note that the energy range of the diffusion coefficients is determined by Equation (5)).

The larger diffusion coefficients, through increasing $\kappa_{\parallel 0}$, cause the Fd magnitude at 1.0 GeV to decrease and the recovery time to increase. These results are generally consistent with previous simulation work by Thomas & Gall (1984) and le Roux & Potgieter (1989, 1991).

Table 2
The Magnitude and Recovery Times for Fd Profiles Shown in Figure 2

Parameter Values	Magnitude	Recovery Time (in days)
$E = 1$ GeV $\kappa_{\parallel 0} = 50 \times 10^{20}$ cm^2 s^{-1}	0.21	2.14
$E = 0.5$ GeV $\kappa_{\parallel 0} = 50 \times 10^{20}$ cm^2 s^{-1}	0.23	2.35
$E = 0.1$ GeV $\kappa_{\parallel 0} = 50 \times 10^{20}$ cm^2 s^{-1}	0.255	2.92
$E = 1$ GeV $\kappa_{\parallel 0} = 20 \times 10^{20}$ cm^2 s^{-1}	0.23	1.18
$E = 1$ GeV $\kappa_{\parallel 0} = 50 \times 10^{20}$ cm^2 s^{-1}	0.21	2.14
$E = 1$ GeV $\kappa_{\parallel 0} = 100 \times 10^{20}$ cm^2 s^{-1}	0.17	3.5

3.2. New Features Revealed by the 3D Model

In this section, we focus on the particular contributions made to the Fd profiles when using this 3D approach.

3.2.1. Effects of the Spatial Extent of the Disturbances

As discussed above, the propagating diffusion barrier model has a 3D configuration, with longitude $\phi_{\rm br}$, latitude $\theta_{\rm br}$, and radial extent L. In what follows, we explore how these geometrical factors affect the characteristic features of the Fd profiles. The default parameter set for these simulations is $A < 0$, $\alpha = 15°$, $\rho = 3.0$, $L = 0.5$, $\theta_{\rm br} = 45°$, $\phi_{\rm br} = 150°$, and $\kappa_\perp/\kappa_\parallel = 0.04$.

Panel (A) in Figure 3 demonstrates the effect on the simulated Fd profiles when varying ρ from 3.0 to 6.0 in Equation (15). It shows that reducing the diffusion coefficients more inside the barrier effectively strengthens the barrier, making it more difficult for cosmic rays to propagate through it. Evidently, as ρ is increased, the Fd magnitude increases accordingly. The magnitude and recovery time (in days) for each individual case are given in Table 3. The Fd magnitude increases nearly linearly with increasing ρ, which directly reflects the reduced diffusion level caused by the barrier.

Qualitatively, this feature can be easily interpreted from the 1D analytical solution by Chih & Lee (1986) which gives

$$\frac{j_0 - j_{\rm m}}{j_0} = \frac{V\left(\frac{\Delta K}{K}\right)L}{K}. \quad (20)$$

It states that the magnitude of this Fd is proportional to the decrease of the diffusion coefficient $\left(\frac{\Delta K}{K}\right)$ inside the barrier. As for the recovery, it should be noted that for different ρ the characteristic recovery time is nearly the same, about two days. A similar conclusion was reached for a 1D numerical model by le Roux & Potgieter (1989), who pointed out that the recovery is not primarily determined by the characteristics of the barrier but rather dominated by the modulation conditions, which the propagation barrier encounters as it moves outward in the heliosphere.

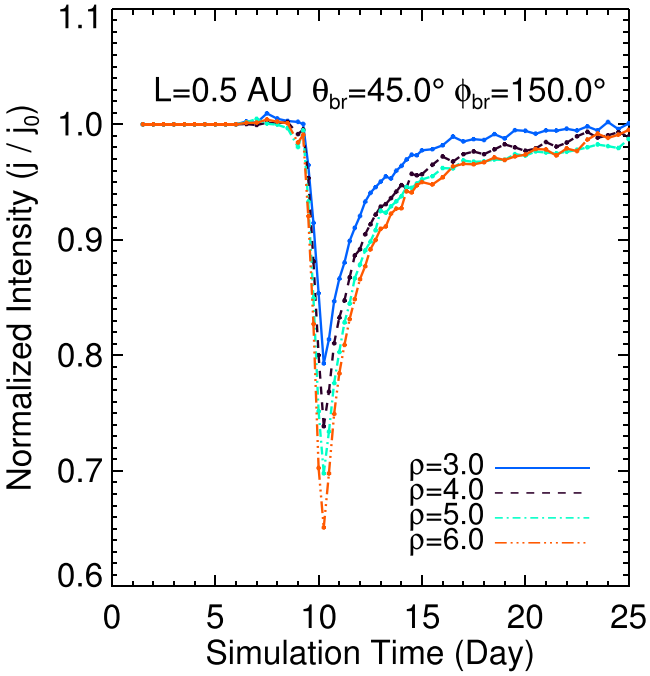

Panel A: Fd profiles for increasing ρ values, while keeping the rest of the parameter set to $L = 0.5$ AU, $\theta_{br} = 45°$, $\phi_{br} = 150°$.

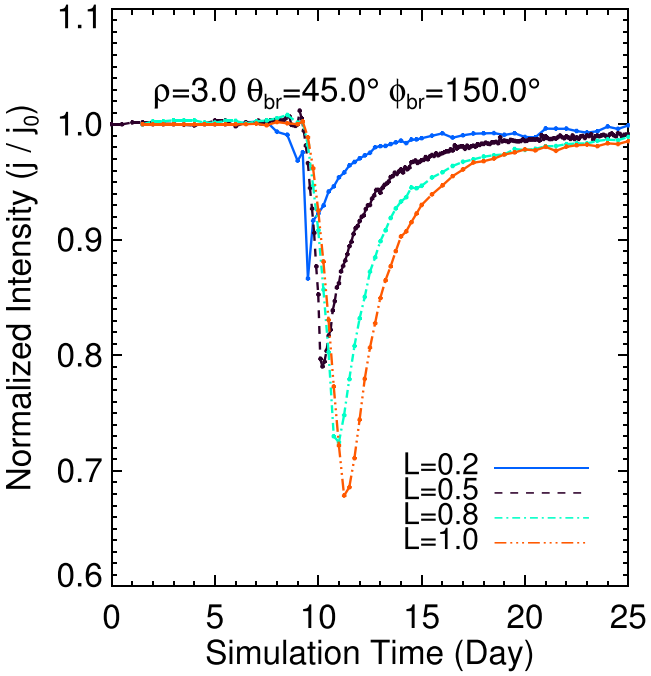

Panel B: Fd profiles for increasing L (au) values, while keeping $\rho = 3.0$, $\theta_{br} = 45°$, $\phi_{br} = 150°$.

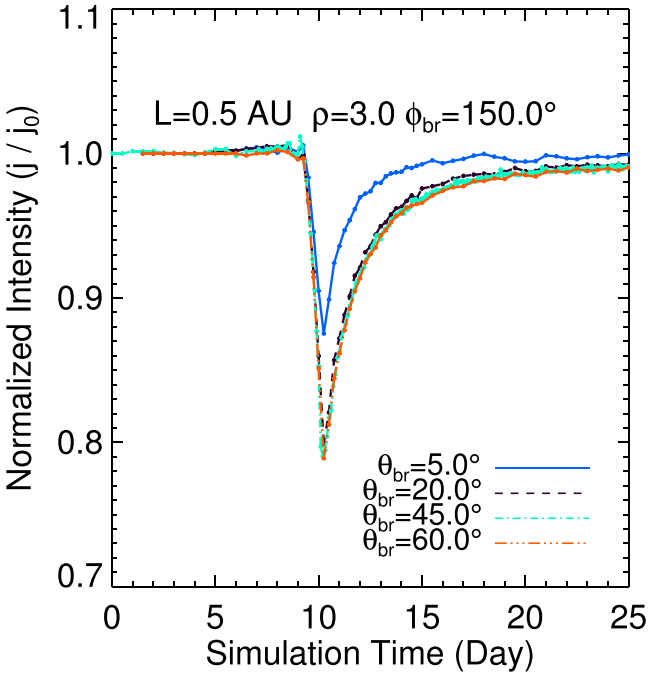

Panel C: Fd profiles when increasing the value of θ_{br} (°), while keeping $L = 0.5$ AU, $\rho = 3.0$, $\phi_{br} = 150°$.

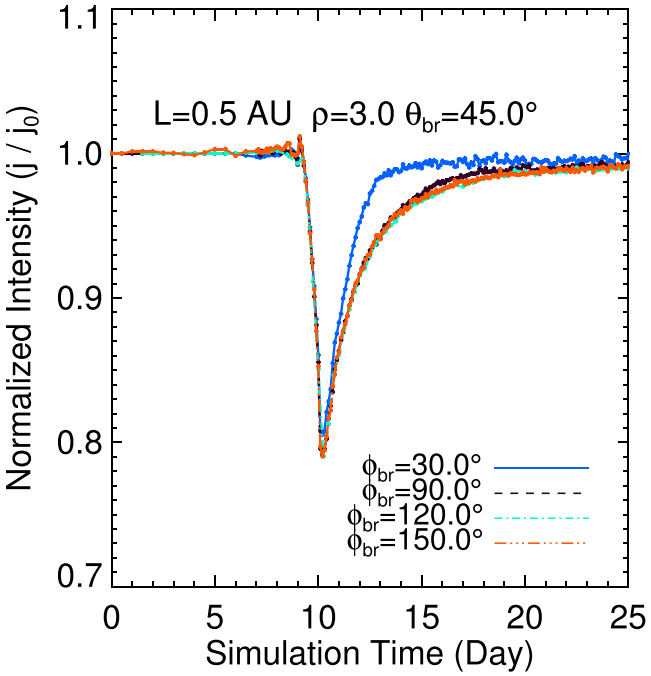

Panel D: Fd profiles for increased ϕ_{br}(°), while keeping $L = 0.5$ AU, $\rho = 3.0$, $\theta_{br} = 45°$.

Figure 3. Fd profiles for changing charateristic parameters. (A) Changing ρ, the level of diffusion inside the barrier. (B) Changing the barrier's width L. (C) Changing the barrier's latitudinal extent through $\theta_{\rm br}$. (D) Changing the barrier's longitudinal extent through $\phi_{\rm br}$.

Table 3
The Magnitude and Recovery Time for the Fd Profiles As Displayed in Figure 3, Panels (A)–(D)

Parameter Values	Magnitude	Recovery Time (days)
$\rho = 3.0$	0.21	1.95
$\rho = 4.0$	0.26	2.20
$\rho = 5.0$	0.30	2.20
$\rho = 6.0$	0.35	2.15
$L = 0.2$ au	0.14	1.52
$L = 0.5$ au	0.21	2.28
$L = 0.8$ au	0.28	2.25
$L = 1.0$ au	0.32	2.55
$\theta_{\rm br} = 5.^\circ0$	0.13	1.318
$\theta_{\rm br} = 20.^\circ0$	0.20	2.004
$\theta_{\rm br} = 45.^\circ0$	0.21	2.289
$\theta_{\rm br} = 60.^\circ0$	0.21	2.178
$\phi_{\rm br} = 30^\circ$	0.20	1.362
$\phi_{\rm br} = 90^\circ$	0.21	2.216
$\phi_{\rm br} = 120^\circ$	0.21	2.243
$\phi_{\rm br} = 150^\circ$	0.21	2.281

Panel (B) illustrates the effect on Fd profiles when varying the width L of the barrier. The Fd magnitude and recovery times are listed in Table 3. Because the location for maximum reduction in the level of diffusion is not at the center of the barrier, the time of maximum intensity decrease shifts as the width of the barrier changes. Similar to the effect of ρ, the barrier's width has a much larger effect on the magnitude of the Fd than on its recovery time. For example, as the barrier's width doubles from 0.5 to 1.0 au, the magnitude increased about 53% while the recovery time only changes about 10%. Qualitatively, this feature also follows from the 1D analytical solution of Chih & Lee (1986) given above.

Our 3D model provides an opportunity to study how the latitude and longitude extent of the propagation barrier may affect the features of the Fd profiles. Panel (C) in Figure 3 depicts the simulation results when only varying the latitudinal extent through changing $\theta_{\rm br}$, while panel (D) displays the results when varying only the longitudinal extent through changing $\phi_{\rm br}$. As illustrated in panel (C) and table 3, the magnitude of the simulated Fd increases as $\theta_{\rm br}$ increases from 5° to 20°, and the recovery time increases as well. However, when the latitude extent become larger than 20°, the effect on the Fd profile caused by $\theta_{\rm br}$ seems to become insignificant. The Fd magnitude only changes about 5% when $\theta_{\rm br}$ increases from 20° to 45°, while the magnitude is nearly the same for $\theta_{\rm br} = 45^\circ$ and $\theta_{\rm br} = 60^\circ$. A similar feature is shown in panel (D), both Fd magnitude and recovery time increase as the longitude extent $\phi_{\rm br}$ increases from 30° to 90°, but for the $\phi_{\rm br} > 90^\circ$ cases, $\phi_{\rm br}$ has an almost negligible effect on the Fd profile. Overall, changing the angular extent of the diffusion barrier has much less effect on the Fd profile than changing its radial width and magnitude of diffusion reduction.

These simulation results can be explained by considering the fact that in 3D the diffusion tensor has three different elements $\kappa_\parallel$, $\kappa_{\perp\theta}$, and $\kappa_{\perp r}$ along different directions. A given location, say at the Earth, will become fully immersed inside the diffusion barrier when it arrives. All three diffusion coefficients are then locally reduced. When varying the latitudinal extent of the barrier, it mainly interferes with the diffusion in the polar direction, mainly through $\kappa_{\perp\theta}$; while changing the longitudinal extent interferes with diffusion in the azimuthal direction, mainly through $\kappa_\parallel$. Changing $\theta_{\rm br}$ or $\phi_{\rm br}$ therefore has fewer effects on the local intensity at the point of observation because this intensity is determined by all three diffusion elements. However, when ρ and L are changed, the diffusion process is affected in all spatial directions and this is reflected in the Fd profile.

It is noted that the simulation results in the panel (D) are somewhat different from those reported by Thomas & Gall (1984), who stated that the Fd would change significantly (especially the recovery profile) if the propagating shock has a full spherical extent. There may be several reasons for this difference because Thomas & Gall (1984) utilized (1) a different treatment of the adiabatic cooling term in the transport equation; (2) the $\kappa_\parallel$ used by them ($\sim 10^{23}$ cm^2 s^{-1}) is larger than ours ($\sim 10^{21}$ cm^2 s^{-1}); and (3) current sheet drift was not included in their model, which is too important to be neglected (le Roux & Potgieter 1989; Potgieter 2014).

3.2.2. The Effects of the Current Sheet Rotation

As a consequence of the solar rotation, the HCS co-rotates and influences cosmic-ray modulation. It is possible to take this rotation into account in the 3D time-dependent model as utilized here. In what follows, we explore and report on how the co-rotation of the wavy HCS affects cosmic-ray modulation and Fd profiles.

As mentioned with Equation (10), the HCS rotating motion can be simulated through an additional term $-\Omega t$ which is added to the projected azimuthal angle ϕ^*. As an initial investigation, we simply treat the solar rotation period to be 27.27 days, which gives an angular speed of $\Omega = 2\pi/27.27$. Figure 4 demonstrates how the HCS rotation affects the intensity profiles. (1) The solid red line is the cosmic-ray intensity at 1 GeV at the Earth after adapting a rotating HCS into the numerical model but without a propagating barrier present. Instead of being a constant over time (undisturbed intensity), it now displays a periodic pattern of which the period coincides with half the solar rotating period, namely $27.27/2 = 13.635$ days. (2) The green dashed line represents the Fd profile for a non-rotating HCS and obviously a propagation barrier causing the Fd as discussed above. (3) The dot dashed blue line represents the Fd profile with a rotating HCS, which now also exhibits the periodic pattern during its recovery phase. This pattern is clearly caused as the barrier crosses the wavy HCS and is rooted in the occurrence of HCS drift. For the $A < 0$ epoch during relative minimum modulation condition ($\alpha = 30^\circ$), cosmic-ray protons drift inward mainly along the equatorial HCS, and as it rotates, the relative location from the Earth to the HCS varies, as is the latitudinal cosmic intensity gradient, resulting in changing thecosmic-ray intensity in a periodic manner as the Earth is above and below the rotating HCS.

In addition, as illustrated in Figure 5, the modeled HCS is symmetric with respect to the Earth's position if the azimuthal angle ϕ^* differs by π, so that the relative location of the Earth with respect to the HCS is the same after the Sun has rotated 180°. This explains why the period for the cosmic-ray intensity curve is exactly half the solar rotation period. However, this perfect symmetry will be disturbed if the Earth is allowed to rotate also in the model. The effects on thecosmic-ray intensity caused by the relative location of the Earth (or any other point

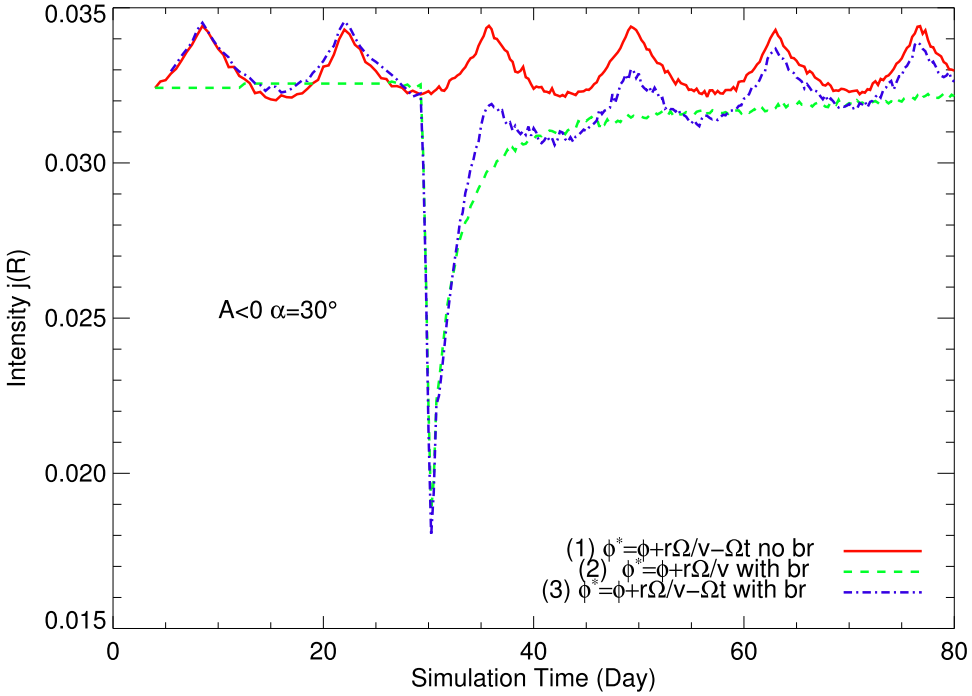

Figure 4. Simulated 1.0 GeV proton intensity by using different HCS models: (1) rotating the HCS without a diffusion barrier, denoted by the solid red line, (2) a non-rotating HCS but with a diffusion barrier present, denoted by the green dashed line, (3) the rotating HCS and a diffusion barrier present, denoted by the dot dashed blue line. The parameter set for these simulations is $A < 0$, $\alpha = 30°$, $L = 0.5$ au, $\rho = 6.0$, $\theta_{\rm br} = 45°$, $\phi_{\rm br} = 150°$, $\kappa_{\|0} = 50 \times 10^{20}$ cm^2 s^{-1}, $\kappa_{\perp 0} = 5 \times 10^{20}$ cm^2 s^{-1}.

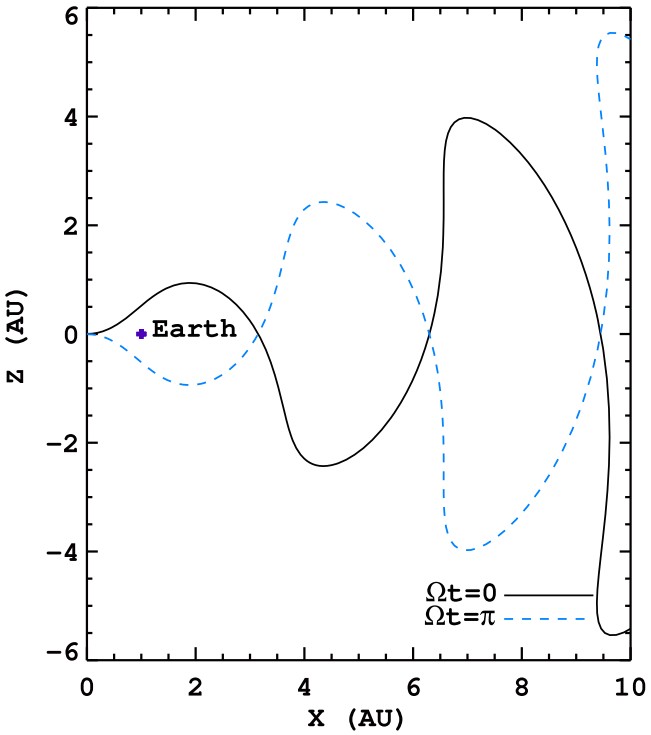

Figure 5. Current sheet profiles along the *X*–*Z* (meridional) plane. Because of the current sheet's rotation, the azimuthal angle ϕ^* differs by π in these two cases. The location of the Earth, in the equatorial plane, is shown in the plot with respect to the location of the HCS for the two mentioned senarios.

of observation) with respect to the HCS was reported before (Barker & Hatton 1971; Antonucci et al. 1978; Levy 1978). What we present here, is how this influences a Fd profile under solar minimum conditions and how it creates a 13.6 day periodicity without having any co-rotating interactions regions present.

3.2.3. Fds at Different Radial Distances

Analysing the cosmic-ray data from Pioneer 10 and 11, Van Allen (1979) found that Fds occurring at the Earth also occur later at different heliocentric radial distances as the assumed corresponding magnetic cloud, as a transient plasmatic disturbance, propagates outward; see also Van Allen & Fillius (1992). Recognizing that these disturbances can be long-lived and radially propagating with the solar wind in the heliosphere, McDonald et al. (1981) argued that Fds should also play a relative role (but never dominating) in the long-term modulation of cosmic rays. In our 3D model the diffusion barrier represents such an outward propagating disturbance, enabling us to obtain Fd profiles as a function of increasing heliocentric radial distances.

Figure 6 illustrates how the magnitude of a simulated Fd changes with increasing heliocentric radial distances (black crosses). In the first place, the Fd magnitude evidently decreases overall with increasing radial distance. It is significantly reduced in the inner heliosphere between 1 and 3 au. Previous 2D numerical simulations (le Roux & Potgieter 1991) and 1D analytical work (Chih & Lee 1986) predicted the same qualitative behavior. As discussed at length by le Roux & Potgieter (1991), this reduction occurs because the value of the undisturbed diffusion coefficients increase as a function of radial distance, thus causing the relative reduced diffusion level ($\frac{\Delta K / K}{K}$ in Equation (20)) inside the barrier to decrease. second, a very interesting feature of our simulated Fd magnitude is that it does not decrease smoothly but exhibits an oscillating pattern in the reduction of its magnitude as the Fd moves outward in the heliosphere. Comparing these magnitude variations with the profile of the wavy HCS plotted in the *XZ*

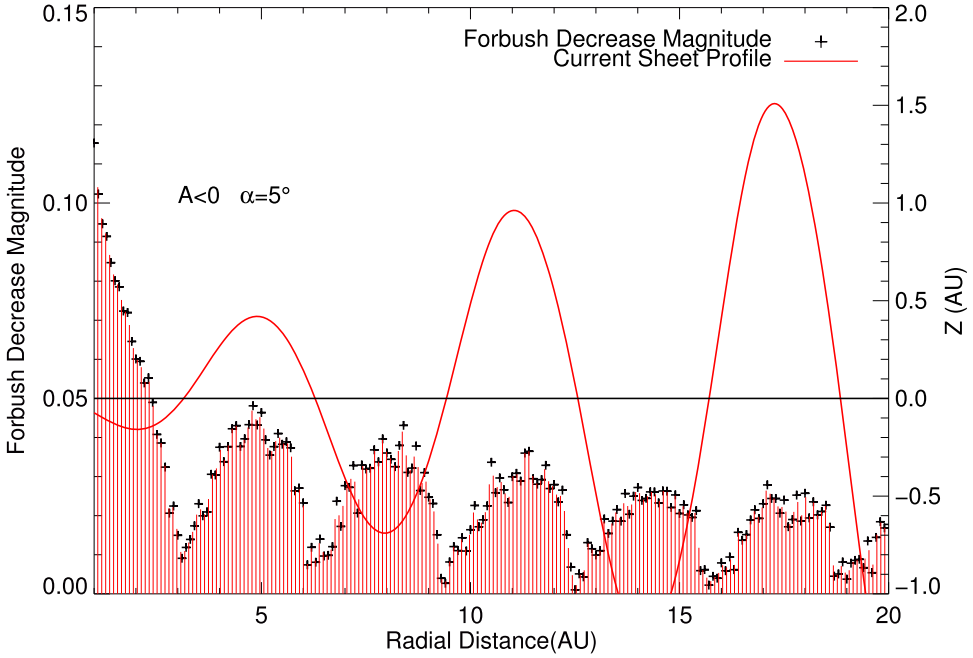

Figure 6. Magnitude of an Fd as a function of increasing heliocentric radial distance (black crosses). The solid red curve represents the HCS profile along the meridional plane. The parameter set for these simulations is $A < 0$, $\alpha = 5°$, $L = 0.5$ au, $\rho = 3.0$, $\theta_{\rm br} = 45°$, $\phi_{\rm br} = 150°$, and $\kappa_{\|0} = 50 \times 10^{20}$ cm^2 s^{-1}.

meridional plane, as shown in this figure, we found that these oscillating patterns correlate very well. The Fd magnitude reaches minimum values at the location where the HCS intersects with the equatorial plane (where the virtual observer is located). The peaks in magnitude variation curve occur when the observer is farthest from the HCS. This feature can be explained by the interplay between the diffusion barrier and the HCS. Near the current sheet, drift dominates the cosmic-ray transport process so that the diffusion barrier has its smallest effect, resulting in a small Fd magnitude. Farther away from the HCS, the effect of the barrier gets larger, causing the Fd magnitude to increase.

It is interesting to look for these predicted features in cosmic-ray observations. It turns out that Webber et al. (1986), who analyzed cosmic-ray data from *IMP*8, *Pioneer* 10, and *Voyagers* 1 & 2 to study about 20 Fd events observed between 1 and 30 au, reported that the magnitude of Fd decreases with increasing radial distance at about 1.5% per au for the period of 1978–1984. They furthermore showed results that displayed a periodicity in the magnitude of Fds as a function of radial distance but did not offer an explanation. This was also shown by le Roux & Potgieter (1989, 1991) who could not simulate this periodicity with their 2D model. As shown in Figure 6, our 3D model is able to simulate such a periodicity.

4. Summary, Conclusions, and Outlook

The SDE method is used to build a full 3D time-dependent, cosmic-ray transport model that includes diffusion, drift, solar wind convection, and adiabatic cooling. The reduced diffusion mechanism is utilized to model a 3D propagating barrier for simulating Fd profiles. This barrier has a complete 3D geometrical shape, which gives it a radial, latitudinal, and longitudinal extent that can be changed in the model.

As a test (validation) of our SDE approach, we first simulate an Fd in comparison with previously published work. The magnitude (or amplitude) and the recovery time for the Fd under different varying conditions, e.g., switching the solar magnetic field polarity, changing the tilt angle of the wavy HCS and the energy of the incoming cosmic rays, our simulation results are found to be consistent with most reported previous numerical simulations.

After validating our 3D model, we continued to study the effects of a full 3D approach, specifically how it affects the features of Fd profiles in terms of its magnitude and recovery times. We find that the two parameters ρ and L, which, respectively, determine the strength (reduced diffusion level) and radial extent of the barrier, have larger effects on the Fd than the other two geometrical parameters $\theta_{\rm br}$ and $\phi_{\rm br}$, the latitudinal and longitudinal extent respectively. We attribute this surprising result to the fact that the diffusion processes in a 3D simulation model happen along three different directions so that $\theta_{\rm br}$ and $\phi_{\rm br}$, which interfere with diffusion only along their specific direction, have a limited effect on the profile of an Fd.

We also investigated how the rotation of the wavy HCS (a true 3D structure) affects the profile of an Fdby, adding a rotational term to the HCS formula. We find that the HCS's rotation gives a periodic pattern in the cosmic-ray intensity at a fixed observation point such as the Earth. It reflects how the Earth's relative location to the HCS affects the cosmic-ray intensity so that both the magnitude and recovery time of an Fd at the Earth change accordingly. The recovery phase of the Fd profile also exhibits this periodicity if the duration of the recovery time is sufficiently long.

The SDE model is furthermore used to simulate Fd profiles at increasing heliocentric radial distance as the diffusion barrier propagates past the Earth and farther outward. We find that (1) overall the Fd magnitude decreases as the radial distance increases, (2) the radial dependence for the Fd magnitude weakens at larger radial distances, and (3) the Fd magnitude oscillates with radial distance. Further analysis demonstrates that the oscillating pattern agrees well with the HCS's wavy profile. This means that the Fd magnitude reaches a minimum value when the barrier is crossing the HCS, indicating that the

HCS drift plays an important part in the main features of Fds, even when solar activity is low.

In summary, we have built a 3D SDE model for simulating Fds and new interesting features are revealed by this 3D approach. As a next step, we plan to study Fd recovery times with the heliocentric radial distance. The propagation speed of the diffusion barrier should also be designed to contain a latitudinal and azimuthal component so that the simulated barrier expands geometrically when propagating outward in the heliosphere. The model predicts that under quiet solar modulation conditions (tilt angles up to $\alpha = 30^{\circ}$), the effect of the HCS should be evidenced in the recovery phase of a single Fd. Such an Fd event occurred in 2006 December (Adriani et al. 2011) and it will be interesting to see if this behavior is evident in the proton observations made by PAMELA (Adriani et al. 2013) or from neutron monitor (cosmic-ray) observations (Zhao & Zhang 2016).

The work is jointly supported by the National Natural Science Foundation of China (41231068, 41304137, 41531073, and 41504132, 11575203) and the Specialized Research Fund for State Key Laboratories. X.L. acknowledges the support of the post-doctoral programme of the North-West University in South Africa. M.S.P. acknowledges the financial support of the South African National Research Foundation (NRF) under the Incentive and Competitive Funding for Rated Researchers, grants 87820 and 68198. M.Z. was supported in part by NASA Grants NNX14AJ53G and NNX15AN72G. This material is based upon work supported by the US National Science Foundation under Grant No. CNS 09-23050.

References

Adriani, O., Barbarino, G. C., Bazilevskaya, G. A., et al. 2011, ApJ, 742, 102
Adriani, O., Barbarino, G. C., Bazilevskaya, G. A., et al. 2013, ApJ, 765, 2
Antonucci, E., Marocchi, D., & Perona, G. E. 1978, ApJ, 220, 712
Arunbabu, K. P., Antia, H. M., Dugad, S. R., et al. 2015, A&A, 580, A41
Barker, M. C., & Hatton, C. J. 1971, P&SS, 19, 549
Barouch, E., & Burlaga, L. F. 1975, JGR, 80, 449
Burger, R. A., & Potgieter, M. S. 1989, ApJ, 339, 501
Cane, H. V. 2000, SSRv, 93, 55
Cheng, A. E., Sarris, E. T., & Dodopoulos, C. 1990, ApJ, 350, 413
Chih, P. P., & Lee, M. A. 1986, JGR, 91, 2903
Engelbrecht, N. E., & Burger, R. A. 2015, AdSpR, 55, 390
Forbush, S. E. 1937, PhRvL, 51, 1108
Forman, M. A., Jokipii, J. R., & Owens, A. J. 1974, ApJ, 192, 535
Jokipii, J. R., Levy, E. H., & Hubbard, W. B. 1977, ApJ, 213, 861
Kadokura, A., & Nishida, A. 1986, JGR, 91, A1
Kopp, A., Büsching, I., Strauss, R. D., & Potgieter, M. S. 2012, CoPhC, 183, 530
Kóta, J., & Jokipii, J. R. 1983, ApJ, 265, 573
le Roux, J. A., & Potgieter, M. S. 1989, AdSpR, 9, 225
le Roux, J. A., & Potgieter, M. S. 1991, A&A, 243, 531
Levy, E. H. 1978, GeoRL, 5, 969
Lockwood, J. A., & Webber, W. R. 1986, JGR, 91, 2851
Lockwood, J. A., Webber, W. R., & Debrunner, H. 1991, JGR, 96, 11587
Luo, X., Zhang, M., Rassoul, K. H., & Pogorelov, N. V. 2011, ApJ, 730, 13
Luo, X., Zhang, M., Rassoul, K. H., Pogorelov, N. V., & Heerikhuisen, J. 2013, ApJ, 764, 85
McDonald, F. B., Trainor, J. H., Lal, N., Van Hollebeke, M. A. I., & Webber, W. R. 1981, ApJL, 249, L71
Morrison, P. 1956, PhRvL, 101, 1397
Mulder, M. S., & Moraal, H. 1986, ApJL, 303, L75
Ngobeni, D. M., & Potgieter, M. S. 2015, AdSpR, 56, 1525
Nishida, A. 1982, JGR, 87, 6003
Parker, E. N. 1965, P&SS, 13, 9
Potgieter, M. S. 2014, AdSpR, 53, 1415
Potgieter, M. S., & Moraal, H. 1985, ApJ, 294, 425
Raath, J. L., Potgieter, M. S., Strauss, R. D., & Kopp, A. 2016, AdSpR, 57, 1965
Sarris, E. T., Dodopoulos, C. A., & Venkatesan, D. 1989, SoPh, 120, 153
Simpson, J. A. 1954, PhRvL, 94, 426
Strauss, R. D., Potgieter, M. S., Büsching, I., & Kopp, A. 2012, Ap&SS, 339, 223
Thomas, B. T., & Gall, R. 1984, JGR, 89, 2991
Van Allen, J. A. 1979, GeoRL, 6, 566
Van Allen, J. A., & Fillius, R. W. 1992, GeoRL, 19, 1423
Wawrzynczak, A., & Alania, V. M. 2010, AdSpR, 45, 622
Webber, W. R., Lockwood, J. A., & Jokipii, J. R. 1986, JGR, 91, 4103
Yu, X. X., Lu, H., Le, G. M., & Shi, F. 2010, SoPh, 263, 223
Yurchyshyn, V., Yashiro, S., Abramenko, V., Wang, H., & Gopalswamy, N. 2005, ApJ, 619, 599
Zhang, G., & Burlaga, L. F. 1988, JGR, 93, 2511
Zhang, M. 1999, ApJ, 513, 409
Zhao, L. L., & Zhang, H. 2016, ApJ, 827, 13